

Ultra-High Energy Cosmic Rays

M.T. Dova

Instituto de Física La Plata, Universidad Nacional de La Plata and CONICET, Argentina

Abstract

The origin of the ultra high energy cosmic rays (UHECR) with energies above $E > 10^{17}$ eV, is still unknown. The discovery of their sources will reveal the engines of the most energetic astrophysical accelerators in the universe. This is a written version of a series of lectures devoted to UHECR at the 2013 CERN-Latin-American School of High-Energy Physics. We present an introduction to acceleration mechanisms of charged particles to the highest energies in astrophysical objects, their propagation from the sources to Earth, and the experimental techniques for their detection. We also discuss some of the relevant observational results from Telescope Array and Pierre Auger Observatory. These experiments deal with particle interactions at energies orders of magnitude higher than achieved in terrestrial accelerators.

1 Introduction

Extreme physical systems provide the best scenario to study the fundamental physical laws. In this direction the research on ultra high energy cosmic rays is a crucial element, contributing to progress in both astrophysics and particle physics. UHECR open a window to energy and kinematic regions previously unexplored in the study of fundamental interactions and continue to motivate current and future cosmic ray experiments. In this note we summarize a series of lectures given at the 7th CERN-Latin-American School of High-Energy Physics on ultra high energy cosmic rays, the highest-energy particles measured on Earth with energy $E > 10^{17}$ eV.

UHECR are mainly protons and nuclei, accelerated in astrophysical objects. The requirements for these objects to be sources of UHECR are quite stringent, as in addition to be able to accelerate to extremely high energies, they should also have the luminosity that can account for the observed fluxes. UHECR must survive during acceleration, escape and propagation through the intergalactic space, losing energy in the interactions with the Infrared/optical (IR/O), Cosmic Microwave Background (CMB) or Radio Background photons. We begin with a brief introduction to cosmic rays. Then, we introduce basic concepts of acceleration mechanisms, and the main energy loss processes for UHECR during propagation. The opacity of the CMB to the propagation of these particles is a key issue in the search for the origin of UHECR, leading to a modification of the energy spectrum and a strong constraint on the proximity of UHECR sources. At this point we give a short description of the main experimental techniques for the detection of UHECR and discuss observational results of the cosmic ray spectrum. UHECR are also deflected in the intergalactic and galactic magnetic fields in the propagation volume, what limits the search for correlations of the arrival direction of UHECR with possible sources and distributions of astrophysical objects in our vicinity. Here we present studies of anisotropy at the highest energies. Next, we summarize the phenomenology of cosmic ray air showers, including the dominant electromagnetic processes driving the shower evolution. We also present the hadronic interaction models used to extrapolate results from collider data to ultrahigh energies. Finally, we describe the main observables sensitive to primary composition, the most challenging issue to understand the nature and origin of UHECR.

2 Cosmic Rays

In 1912, Victor Hess carried out a series of balloon flights taking an electroscope to measure the ionizing radiation as a function of altitude. He discovered that the ionization rate increased by at least a factor

of two at around 5 km above the Earth’s surface [1]. He received the Nobel prize in 1936 for the discovery of this “penetrating radiation” coming from space, later called cosmic rays. In 1938, Pierre Auger and his colleagues first reported the existence of extensive air showers (EAS), showers of secondary particles caused by the collision of primary high energy particles with air molecules. On the basis of his measurements, Auger concluded that he had observed showers with energies of 10^{15} eV [2, 3]. The literature abounds in historical introductions to cosmic rays, we recommend the heart-warming notes by J. Cronin at the 30th International Cosmic Ray Conference [4]. See also the lectures notes presented in Refs. [5, 6].

For primary energy above 10^{11} eV, the observed cosmic ray flux can be described by a series of power laws with the flux falling about three orders of magnitude for each decade increase in energy. Figure 1 shows the “all-particle” spectrum. The differential energy spectrum has been multiplied by $E^{2.6}$ in order to display the features of the steep spectrum that are otherwise difficult to discern [7]. A change of the spectral index ($E^{-2.7}$ to $E^{-3.0}$) at an energy of about 10^{15} eV is known as the cosmic ray knee. This feature is generally believed to correspond to the steepening of the galactic proton spectrum, either because a change of the propagation regime or because of maximum limitations at the source, [8–10]. The same effect for heavier nuclei may cause the softer spectrum above the knee. In this context, subsequent steepenings of the spectrum are predicted at $E_{max} \sim Z \times 10^{15}$ eV reaching $\sim 8 \times 10^{16}$ eV for the iron group. The KASCADE-Grande collaboration provided the first observation of this sequence of changes [11]. Above several $\sim 10^{18}$ eV the magnetic field in the vicinity of the Galaxy would not trap very effectively even the very heaviest nuclei, so the detected cosmic rays must be extragalactic [12]. The onset of an extragalactic contribution could be indicated by the so-called second knee, a further steepening of the spectrum at about $10^{17.7}$ eV. The flattening around $10^{18.5}$ eV is called the ankle of the spectrum. The simplest way of producing this feature is that of intersecting the steep galactic spectrum with a flatter extragalactic one. Under this assumption, several models have been developed. In the “ankle model” [13, 14], the transition appears at $10^{18.5}$ eV. This model needs a new high energy galactic component between the iron knee and the onset of the extragalactic component. In the “dip model”, the ankle appears as an intrinsic part of the pair-production dip, a feature predicted in the spectrum of extragalactic protons that can be directly linked to the interaction of UHECR with the CMB [15–17]. In this model the transition from the galactic to the extragalactic component begins at the second knee and is completed at the beginning of the dip at $E \sim 10^{18}$ eV. In “mix composition models” [18], the transition occurs at 3×10^{18} eV with mass composition changing from the galactic iron to extragalactic mixed composition of different nuclei. For a recent comprehensive review of the transition models see Ref. [19].

The Large Hadron Collider (LHC) will collide in 2015 protons at $\sqrt{s} \simeq 14$ TeV. This impressive energy is still about a factor of 50 smaller than the centre-of-mass energy of the highest energy cosmic ray so far observed, assuming primary protons.

For cosmic ray energies above 10^{15} eV, the flux becomes so low that direct detection of the primary using devices in or above the upper atmosphere is, for all practical purposes, impossible. Fortunately, in such cases the primary particle has enough energy to initiate a particle cascade in the atmosphere large enough that the products are detectable at ground. There are several techniques which can be employed in detecting these extensive air showers (EAS), ranging from sampling of particles in the cascade to measurements of fluorescence, Čerenkov or radio emissions produced by the shower.

3 Acceleration of cosmic rays

There are two types of mechanisms able to accelerate charged particles to reach ultrahigh energies and at the same time give a power law injection spectrum. One is the acceleration of particles directly to very high energy by an extended electric field [20], such as the case of unipolar inductors in relativistic magnetic rotators (e.g. neutron stars [21]) or black holes with magnetized disks that lose rotational energy in jets. They have the advantage of being fast, however, they suffer from the circumstance that

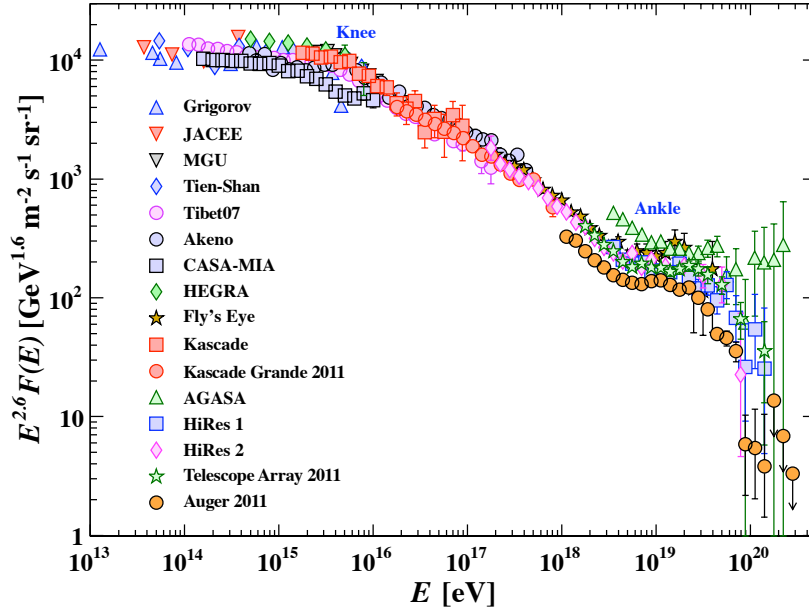


Fig. 1: All-particle spectrum of cosmic rays. From Ref. [7]

the acceleration occurs in astrophysical sites of very high energy density, where new opportunities for energy loss exist. In addition, they predict a hard injection spectrum that cannot be reconciled with the currently observed slope. In 1949, Fermi introduced a statistical acceleration mechanism [22]. In his publication, Fermi considered the scattering of cosmic particles on moving magnetized clouds which led to a fractional energy gain $\xi = \langle \Delta E \rangle / E \propto \beta^2$ where β is the average velocity of the scattering centres in units of c . There is a net transfer of the macroscopic kinetic energy from the moving cloud to the particle, but the average energy gain is very small. Nowadays, this process is called “second order Fermi acceleration”. The first really successful theory of high energy cosmic ray acceleration was identified in [23] to be the Fermi acceleration in nonrelativistic shock waves in supernova remnants. The diffusion of cosmic rays in moving magnetized plasmas in the upstream and downstream of the shocks, force particles to repeatedly cross the shock front, hence gaining energy by numerous encounters, this results in $\xi \propto \beta$. When measured in the stationary upstream frame, β is the speed of the shocked fluid in units of c . This mechanism is known as “first order Fermi acceleration”. Shock waves for UHECR acceleration are Gamma Ray Bursts (GRB) shocks, jets and hot spots of Active Galactic Nuclei (AGN), and gravitational accretion shocks.

Following [24], we provide here a simple calculation to obtain the power law predictions from first order Fermi processes under the “test particle approximation”, in which the back-reaction of accelerated CRs on the shock properties is neglected. The energy E_n of a cosmic particle after n acceleration cycles is:

$$E_n = E_0(1 + \xi)^n \quad (1)$$

and the number of cycles to reach E results from Eq. (1)

$$n = \ln \left(\frac{E}{E_0} \right) / \ln(1 + \xi) \quad (2)$$

where E_0 is the energy at injection into the acceleration site. If the escape probability P_{esc} per encounter

is constant, then the probability to stay in the acceleration region after n cycles is $(1 - P_{esc})^n$. The fraction of particles accelerated to energies $> E$, the integral spectrum, is:

$$N(> E) \propto \frac{(1 - P_{esc})^n}{P_{esc}} \propto \frac{1}{P_{esc}} \left(\frac{E}{E_0} \right)^{-\gamma} \quad (3)$$

with $\gamma \propto P_{esc}/\xi$ for $\xi \ll 1$ and $P_{esc} \ll 1$. Note that both first and second order Fermi acceleration produce a power law energy spectrum.

The escape probability from the acceleration site depends on the characteristic time for the acceleration cycle and the characteristic time for escape from the acceleration site. In the rest frame of the shock the conservation relations imply that the upstream velocity u_{up} is much higher than the downstream velocity u_{down} . The compression ratio $r = u_{up}/u_{down} = n_{down}/n_{up}$ can be determined by requiring continuity of particle number, momentum, and energy across the shock. Here n_{up} (n_{down}) is the particle density of the upstream (downstream) plasma. For an ideal gas the compression ratio can be related to the specific heat ratio and the Mach number of the shock. In the case of highly supersonic shocks, $r = 4$ [25]. To determine the spectrum we need to calculate γ . For the case of shock acceleration, $\xi = 4\beta/3 = 4(u_{up} - u_{down})/3$ and the escape probability can be obtained as the ratio of the loss flux, downstream away from the shock, and the crossing flux. Assuming the configuration of a large, plane shock the escape probability results as $P_{esc} = 4u_{down}/c$. Finally, we obtain the spectral index of the integral energy spectrum:

$$\gamma \propto P_{esc}/\xi \propto \frac{3}{u_{up}/u_{down} - 1} \propto 1 \quad (4)$$

This injection spectrum should be compared with the observed flux of cosmic rays, $dN/dE \propto E^{-2}$. The result is in good agreement although additional effects, like energy losses or an energy dependence of the escape probability, could have an important impact on the shape of the injection spectrum. For a comprehensive review of shock acceleration theory, see Ref. [25]. For a discussion about different acceleration mechanisms we recommend Ref. [26].

The requirements for astrophysical objects to be sources of UHECR are stringent. The Larmor radius of a particle with charge Ze increases with its energy E according to

$$r_L = \frac{1.1}{Z} \left(\frac{E}{10^{18} \text{eV}} \right) \left(\frac{B}{\mu\text{G}} \right)^{-1} \text{ kpc}. \quad (5)$$

The search for UHECR extragalactic sources was motivated by the fact that r_L in the galactic magnetic field is much larger than the thickness of the galactic disk, hence, confinement in the galaxy is not maintained for UHECR. The famous Hillas criteria states that the Larmor radius of the accelerated particles cannot exceed the size of the source (R_{source}), setting a natural limit in the particle's energy.

$$E_{\text{max}} \simeq Z \left(\frac{B}{\mu\text{G}} \right) \left(\frac{R_{\text{source}}}{\text{kpc}} \right) \times 10^{18} \text{ eV}. \quad (6)$$

This limitation in energy can be seen in the so-called Hillas plot [27] shown in Fig. 2 where candidate sources are placed in a plane of the characteristic magnetic field B versus their characteristic size R . For protons, the only sources for the UHECR that seem to be plausible are radio galaxy lobes and clusters of galaxies. Exceptions may occur for sources which move relativistically in the host-galaxy frame, in particular jets from AGN and GRB. In this case the maximal energy might be increased due to a Doppler boost by a factor ~ 30 or ~ 1000 , respectively. For a survey of cosmic ray sources shown in Fig. 2 and their signatures, see Refs. [26, 28]. An interesting point is that if acceleration takes place in GRB, one may expect a strong neutrino signature due to proton interactions with the radiative background [29]. Such a signature is now being probed by the Ice Cube experiment [30].

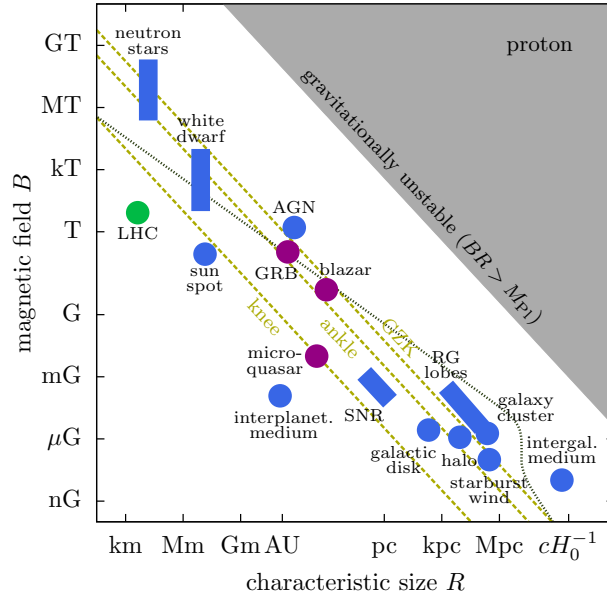


Fig. 2: The “Hillas plot” for various CR source candidates (blue). Also shown are jet-frame parameters for blazars, gamma-ray bursts, and microquasars (purple). The corresponding point for the LHC beam is also shown. The red dashed lines show the *lower limit* for accelerators of protons at the CR knee ($\sim 10^{14.5}$ eV), CR ankle ($\sim 10^{18.5}$ eV) and the GZK suppression ($\sim 10^{19.6}$ eV). The dotted gray line is the *upper limit* from synchrotron losses and proton interactions in the cosmic photon background ($R \gg 1$ Mpc). From Ref. [31].

4 Propagation of extragalactic cosmic rays

4.1 Energy losses of protons

There are three main energy loss processes for protons propagating over cosmological distances: Adiabatic energy losses due to the expansion of the universe, $-dE/dt = H_0 E$, pair production ($p\gamma \rightarrow pe^+e^-$) and pion-production $p\gamma \rightarrow \pi N$ on photons of the cosmic microwave background (CMB). Collisions with optical and infrared photons give a negligible contribution.

The fractional energy loss due to interactions with the cosmic background radiation at a redshift $z = 0$ is determined by the integral of the nucleon energy loss per collision multiplied by the probability per unit time for a nucleon collision in an isotropic gas of photons [32]. For interactions with a blackbody field of temperature T , the photon density is that of a Planck spectrum, so the fractional energy loss is given by

$$-\frac{1}{E} \frac{dE}{dt} = -\frac{ckT}{2\pi^2\Gamma^2(c\hbar)^3} \sum_j \int_{\omega_{0j}}^{\infty} d\omega_r \sigma_j(\omega_r) y_j \omega_r \ln(1 - e^{-\omega_r/2\Gamma kT}), \quad (7)$$

where ω_r is the photon energy in the rest frame of the nucleon, and y_j is the inelasticity, *i.e.* the average fraction of the energy lost by the photon to the nucleon in the laboratory frame for the j th reaction channel. The sum is carried out over all channels and $d\omega$, $\sigma_j(\omega_r)$ is the total cross section of the j th interaction channel, Γ is the usual Lorentz factor of the nucleon, and ω_{0j} is the threshold energy for the j th reaction in the rest frame of the nucleon.

At energies $E \ll m_e m_p/kT = 2.1 \times 10^{18}$ eV, the reaction ($p\gamma \rightarrow pe^+e^-$) takes place on the photons from the high energy tail of the Planck distribution. The cross section of the reaction approximated by the threshold values is $\sigma(\omega_r) = \frac{\pi}{12} \alpha r_0^2 \left(\frac{\omega_r}{m_e} - 2\right)^3$, α is the fine structure constant and r_0 is the classical radius of the electron [33]. The inelasticity at threshold results $y = 2 \frac{m_e}{m_p}$. The fractional

energy loss due to pair production is then,

$$-\frac{1}{E} \left(\frac{dE}{dt} \right) = \frac{16c}{\pi} \frac{m_e}{m_p} \alpha r_0^2 \left(\frac{kT}{hc} \right)^3 \left(\frac{\Gamma kT}{m_e} \right)^2 \exp\left(-\frac{m_e}{\Gamma kT}\right). \quad (8)$$

At higher energies ($E > 10^{19}$ eV) the photopion reactions $p\gamma \rightarrow p\pi^0$ and $p\gamma \rightarrow \pi^+n$ on the tail of the Planck distribution give the main contribution to proton energy loss. The photons are seen blue-shifted by the cosmic rays in their rest frames and the reaction becomes possible. The cross sections of these reactions are well known. It strongly increase at the $\Delta(1232)$ resonance, which decays into the one pion channels π^+n and π^0p at a photon energy in the proton rest frame of 145 MeV. At higher energies, heavier baryon resonances occur and the proton might reappear only after successive decays of resonances. The cross section in this region can be described by a sum of Breit-Wigner distributions over the main resonances produced in $N\gamma$ collisions with πN , $\pi\pi N$ and $K\Lambda$ ($\Lambda \rightarrow N\pi$) final states [34]. For the cross section at high energies the fits from the CERN-HERA and COMPAS Groups to the high-energy $p\gamma$ cross section [35] can be used. Assuming that reactions mediated by baryon resonances have spherically symmetric decay angular distributions, the average energy loss of the nucleon after n resonant collisions is given by

$$y_\pi(m_{R_0}) = 1 - \frac{1}{2^n} \prod_{i=1}^n \left(1 + \frac{m_{R_i}^2 - m_M^2}{m_{R_{i-1}}^2} \right), \quad (9)$$

where m_{R_i} denotes the mass of the i^{th} resonant system of the decay chain, m_M the mass of the associated meson, $m_{R_0} = \sqrt{s}$ is the total energy of the reaction in the c.m., and m_{R_n} the mass of the nucleon. It is well established from experiments that, at very high energies ($\sqrt{s} > 3$ GeV), the incident nucleons lose one-half their energy via pion photoproduction independent of the number of pions produced (“leading particle effect”) [36].

A fit to Eq. (7) for the region $\sqrt{s} < 2$ GeV with the exponential behavior derived from the values of cross section and fractional energy loss at threshold, gives [37]

$$-\frac{1}{E} \left(\frac{dE}{dt} \right)_\pi = A \exp[-B/E], \quad (10)$$

$$A = (3.66 \pm 0.08) \times 10^{-8} \text{ yr}^{-1}, \quad B = (2.87 \pm 0.03) \times 10^{11} \text{ GeV}. \quad (11)$$

The fractional energy loss at higher c.m. energies ($\sqrt{s} \gtrsim 3$ GeV) is roughly a constant,

$$-\frac{1}{E} \left(\frac{dE}{dt} \right)_\pi = C = (2.42 \pm 0.03) \times 10^{-8} \text{ yr}^{-1}. \quad (12)$$

From the values determined for the fractional energy loss, it is straightforward to compute the energy degradation of UHECRs in terms of their flight time. This is given by,

$$At - \text{Ei}(B/E) + \text{Ei}(B/E_0) = 0, \quad \text{for } 10^{10} \text{ GeV} \lesssim E \lesssim 10^{12} \text{ GeV}, \quad (13)$$

and

$$E(t) = E_0 \exp[-Ct], \quad \text{for } E \gtrsim 10^{12} \text{ GeV}, \quad (14)$$

where Ei is the exponential integral. Figure 3 shows the proton energy degradation as a function of the mean propagation distance. Notice that, independent of the initial energy of the nucleon, the mean energy values approach 10^{20} eV after a distance of ≈ 100 Mpc. This fact constrains the proximity to the Earth of the sources of UHECR with energies above 5×10^{19} eV.

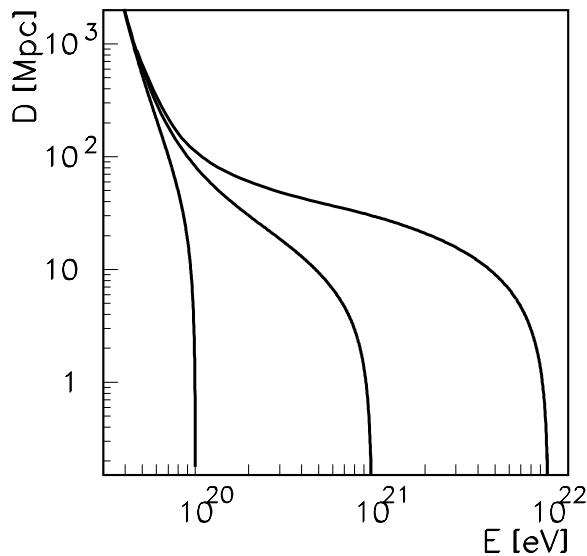


Fig. 3: Energy attenuation length of protons in the intergalactic medium. For proton sources beyond ≈ 100 Mpc, the observed proton energy is $< 10^{20}$ eV regardless its initial value. From Ref. [37].

4.2 Energy losses of nuclei

The relevant mechanisms for the energy loss of nuclei during propagation are: Compton interactions, pair production in the field of the nucleus, photodisintegration and hadron photoproduction. For nuclei of energy $E > 10^{19}$ eV the dominant loss process is photodisintegration. In the nucleus rest-frame, pair production has a threshold at ~ 1 MeV, photodisintegration is particularly important at the peak of the giant dipole resonance (15 to 25 MeV), and photomeson production has a threshold energy of ~ 145 MeV. Compton interactions result in only a negligibly small energy loss for the nucleus [38].

For a nucleus of mass A and charge Ze , the energy loss rate due to photopair production is Z^2/A times higher than for a proton of the same Lorentz factor [39], whereas the energy loss rate due to photomeson production remains roughly the same. The latter is true because the cross section for photomeson production by nuclei is proportional to the mass number A [40], while the inelasticity is proportional to $1/A$. However, it is photodisintegration rather than photopair and photomeson production that determines the energetics of ultrahigh energy cosmic nuclei. During this process some fragments of the nuclei are released, mostly single neutrons and protons. Experimental data of photonuclear interactions are consistent with a two-step process: photoabsorption by the nucleus to form a compound state, followed by a statistical decay process involving the emission of one or more nucleons.

The disintegration rate with production of i nucleons is given by [41]

$$R_{Ai} = \frac{1}{2\Gamma^2} \int_0^\infty dw \frac{n(w)}{w^2} \int_0^{2\Gamma w} dw_r w_r \sigma_{Ai}(w_r) \quad (15)$$

where $n(w)$ is the density of photons with energy w in the system of reference in which the cosmic microwave background (CMB) is at 2.7 K and w_r is the energy of the photons in the rest frame of the nucleus. As usual, Γ is the Lorentz factor and σ_{Ai} is the cross section for the interaction.

Here, the soft photon background is taken as the sum of a 2.7 K Planckian spectrum that dominates at energies $w \in (2.0 \times 10^{-6} \text{ eV}, 4 \times 10^{-3} \text{ eV})$, and the infrared radiation as estimated in Ref. [42]. Parameterizations of the photodisintegration cross section for the different nuclear species are given in Ref. [38]. Summing over all possible channels for a given number of nucleons, one obtains the effective nucleon loss rate $R = \sum_i i R_{Ai}$. The effective nucleon loss rate for light elements, as well as for those in

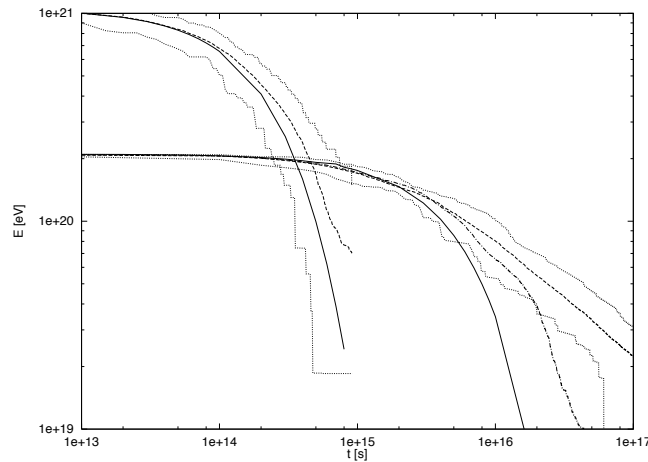


Fig. 4: The energy of the surviving fragment ($\Gamma_0 = 4 \times 10^9$, $\Gamma_0 = 2 \times 10^{10}$) vs. propagation time obtained using Eq. (20) is indicated with a solid line. Also included is the energy attenuation length obtained from Monte Carlo simulations with (dashed) and without (dotted-dashed) pair creation production, for comparison. The region between the two dotted lines includes 95% of the simulations. This gives a clear idea of the range of values which can result from fluctuations from the average behaviour.

the carbon, silicon and iron groups can be scaled as in [38]

$$\left. \frac{dA}{dt} \right|_A \sim \left. \frac{dA}{dt} \right|_{\text{Fe}} \left(\frac{A}{56} \right) = R|_{\text{Fe}} \left(\frac{A}{56} \right), \quad (16)$$

with the photodisintegration rate parametrized by [43]

$$R_{56}(\Gamma) = 3.25 \times 10^{-6} \Gamma^{-0.643} \exp(-2.15 \times 10^{10}/\Gamma) \text{ s}^{-1} \quad (17)$$

for $\Gamma \in [1.0 \times 10^9, 36.8 \times 10^9]$, and

$$R_{56}(\Gamma) = 1.59 \times 10^{-12} \Gamma^{-0.0698} \text{ s}^{-1} \quad (18)$$

for $\Gamma \in [3.68 \times 10^{10}, 10.0 \times 10^{10}]$.

For photodisintegration, the averaged fractional energy loss results equal to the fractional loss in mass number of the nucleus, because the nucleon emission is isotropic in the rest frame of the nucleus. During the photodisintegration process the Lorentz factor of the nucleus is conserved, unlike the cases of pair production and photomeson production processes which involve the creation of new particles that carry off energy. The total fractional energy loss is then

$$-\frac{1}{E} \frac{dE}{dt} = \frac{1}{\Gamma} \frac{d\Gamma}{dt} + \frac{R}{A}. \quad (19)$$

For $\omega_r \lesssim 145$ MeV the reduction in Γ comes from the nuclear energy loss due to pair production [44]. For $\Gamma > 10^{10}$ the energy loss due to photopair production is negligible, and thus

$$E(t) \sim 938 A(t) \Gamma \text{ MeV} \sim E_0 e^{-R(\Gamma)|_{\text{Fe}} t/56}. \quad (20)$$

Figure 4 shows the energy of the heaviest surviving nuclear fragment as a function of the propagation time, for initial iron nuclei. The solid curves are obtained using Eq. (20), whereas the dashed and dotted-dashed curves are obtained by means of Monte Carlo simulations [45]. One can see that nuclei

with Lorentz factors above 10^{10} cannot survive for more than 10 Mpc. For these distances, the approximation given in Eq. (20) always lies in the region which includes 95% of the Monte Carlo simulations. When the nucleus is emitted with a Lorentz factor $\Gamma_0 < 5 \times 10^9$, pair production losses start to be relevant, significantly reducing the value of Γ as the nucleus propagates distances of $\mathcal{O}(100 \text{ Mpc})$. The effect has a maximum for $\Gamma_0 \approx 4 \times 10^9$ but becomes small again for $\Gamma_0 \leq 10^9$, for which appreciable effects only appear for cosmological distances ($> 1000 \text{ Mpc}$), see for instance Ref. [45].

Note that Eq. (20) imposes a strong constraint on the location of nucleus-sources: less than 1% of iron nuclei (or any surviving fragment of their spallations) can survive more than $3 \times 10^{14} \text{ s}$ with an energy $> 10^{20.5} \text{ eV}$. It is important to keep in mind that a light propagation distance of $1.03 \times 10^{14} \text{ s}$ corresponds to 1 Mpc.

In recent years the interest in the propagation of UHECR nuclei has significantly grown. A complete review with a detailed list of references can be found in [46]. Most recent calculations of UHECR proton propagation use the Monte Carlo generator SOPHIA [47] for photomeson interaction of protons, based on available data and phenomenological models. For the case of nuclei propagation, existing propagation codes are CRPropa [48] and the complete nuclei propagation tool presented in Ref. [49].

5 Cosmic ray observations at the highest energies: Hybrid instruments

For primary cosmic ray energies above 10^{14} eV , the flux becomes so low that individual events cannot longer be detected directly. Fortunately, in such cases the primary particle has enough energy to initiate an extended air shower (EAS) in the atmosphere. Only the secondary particles are detected and used to infer the properties of the primary particle. There are several techniques which can be employed in detecting EAS.

The most commonly used detection method involves sampling the shower front at a given altitude using an array of sensors spread over a large area. The classical set up consists of an array of plastic scintillators, registering charged particles from the shower (also some converted photons). Another technique is to use water Čerenkov detectors (WCD), that allow the detection of the very numerous photons present in showers. They are deep compare with scintillators, so they have larger response to inclined showers. An initial estimate of the shower direction is obtained from the relative arrival times of signal at a minimum of 3 non-collinear detectors, treating the shower front as if it were planar. The density of particles falls off with the distance to the shower core and this can be parameterized by a lateral distribution function (LDF), which, of course, depends on the characteristics of the detectors used. The particle density at a large distance from the shower core is commonly used as an energy estimator. Muons in the EAS have higher energies than electromagnetic particles, which in addition suffer significant scattering and energy loss. Thus, the muonic component tends to arrive earlier and over a shorter period of time than the electromagnetic one. These signatures may also help to distinguish μ 's from electrons and γ 's providing a useful tool to determine the primary composition.

Another highly successful air shower detection method involves measurement of the longitudinal development of the cascade by sensing the fluorescence light produced via interactions of the charged particles in the atmosphere. As an extensive air shower develops, it dissipates much of its energy by exciting and ionizing air molecules along its path. Excited nitrogen molecules fluoresce producing radiation in the 300 - 400 nm ultraviolet range, to which the atmosphere is quite transparent. Under favourable atmospheric conditions EAS can be detected at distances as large as 20 km, though observations can only be made on clear moonless nights, yielding a duty cycle of about 10%. The shower development appears as a rapidly moving spot of light whose angular motion depends on both the distance and the orientation of the shower axis. The fluorescence technique provides the most effective way to measure the energy of the primary particle. The amount of fluorescence light emitted is proportional to the number of charged particles in the showers allowing a direct measurement of the longitudinal development of the EAS in the atmosphere. For this, the sky is viewed by many segmented eyes using photomultipliers. From the

measured shower profile the position of the shower maximum X_{max} , which is sensitive to primary composition, can be obtained. The energy in the electromagnetic component is calculated by integrating the measured shower profile, after corrections for atmospheric attenuation of the fluorescence light and contamination of the signal by Čerenkov light. Finally, to derive the total energy of the shower, an estimate of the missing energy carried to the ground by neutrinos and high energy muons must be made based on assumptions about the primary mass and the appropriate hadronic interaction models.

In this note we focus on the two high energy cosmic ray experiments currently operating: the Pierre Auger Observatory [50] and the Telescope Array (TA) [51]. The Pierre Auger Observatory, the largest UHECR experiment in the world, is located in Malargüe, Argentina ($35^{\circ}12'S$, $69^{\circ}12'W$). It has an accumulated exposure of about $30000 \text{ km}^2 \text{ sr yr}$. The Telescope Array located in Millard County, Utah, USA ($39.3^{\circ}N$, $112.9^{\circ}W$), due to a later start and its more than 4 times smaller area, has collected about 10 times less events. Both the Pierre Auger Observatory and TA are hybrid detectors employing two complementary detection techniques for the ground-based measurement of air showers induced by UHECR: a surface detector array (SD) and a fluorescence detector (FD).

The ground array of the Pierre Auger Observatory consists of 1600 stations spaced by 1.5 km covering an area of 3000 km^2 . Each detector is a cylindrical, opaque tank of 10 m^2 and a water depth of 1.2 m, where particles produce light by Čerenkov radiation. The filtered water is contained in an internal coating which diffusely reflects the light collected by three photomultipliers (PMT) installed on the top. The large diameter PMTs ($\approx 20 \text{ cm}$) hemispherical photomultiplier are mounted facing down and look at the water through sealed polyethylene windows that are integral part of the internal liner. Due to the size of the array the stations have to work in an autonomous way. Thus the stations operate on battery-backed solar power and communicate with a central station by using wireless LAN radio links. The time information is obtained from the Global Positioning Satellite (GPS) system. This array is fully efficient at energies above $E > 3 \times 10^{18} \text{ eV}$. Additional detectors with 750 m spacing have been nested within the 1500 m array to cover an area of 25 km^2 with full efficiency above $E > 3 \times 10^{17} \text{ eV}$. The SD is sensitive to electromagnetic and muonic secondary particles of air showers and has a duty cycle of almost 100%. The surface array is overlooked by 27 optical telescopes grouped in 5 buildings on the periphery of the array [52]. The field of view of each telescope is 30° in azimuth, and 1.5° to 30° in elevation, except for three of them, for which the elevation is between 30° and 60° (HEAT telescopes [53]). Light is focused with a spherical mirror of 13 m^2 on a camera of 440 hexagonal PMTs. The FD can only operate during dark nights, which limits its duty cycle to 13%. Stable data taking with the SD started in January 2004 and the Observatory has been running with its full configuration since 2008.

In Figure 5 (left panel) we present a schematic description of a water Čerenkov detector installed at the Pierre Auger Observatory. Mounted on top of the tank are the solar panel, electronic enclosure, mast, radio antenna and GPS antenna for absolute and relative timing. A battery is contained in a box attached to the tank. The main components of a fluorescence eye are shown on the right panel of Figure 5: a large spherical mirror with a radius of curvature of 3.4 m, a pixel camera in the focal surface and a diaphragm with an entrance glass window. This filter allows reduction of night background with respect to the fluorescence signal and also serves to protect the equipment from dust.

The TA surface array consists of 507 detector units deployed in a square grid with 1.2 km spacing to cover a total area of approximately 700 km^2 . Each unit consists of a plastic scintillation counter of 3 m^2 surface and 1.2 cm thickness, with 2 layers of plastic scintillators viewed by PMT at each end. The entire system is powered by a solar panel and battery. The communication is done with WLAN modem. The SD array is fully efficient for cosmic rays with energies greater than $10^{18.8} \text{ eV}$ [54]. Three FD stations are placed around the SD array, with a total of 38 telescopes. Each telescope is comprised of a cluster of photo-tubes and a reflecting mirror of 3.3 m diameter. A PMT camera consisting of 16×16 PMTs is set at a distance of 3000 mm from the mirror. The field of view of each PMT is approximately 1° and that of the FD station is from 3° to 33° in elevation and 108° in azimuth. See Ref. [51] for details of the TA detectors.

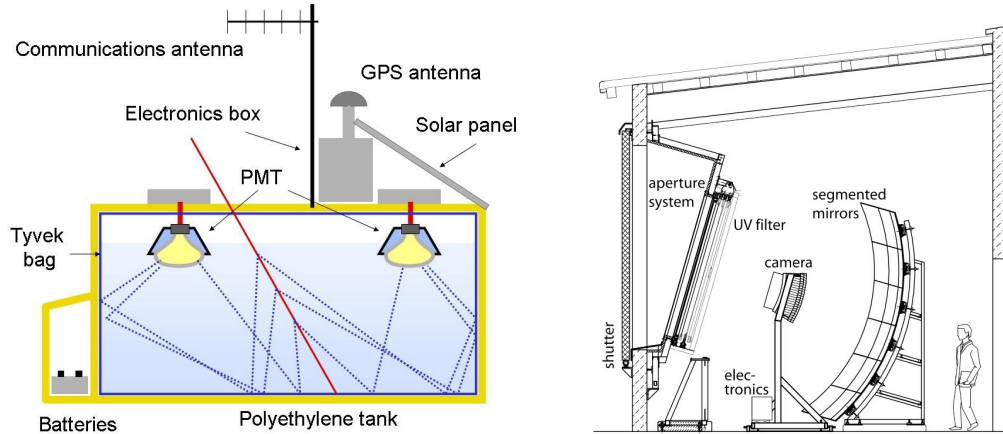


Fig. 5: Left: A typical surface detector of the Auger Observatory. Right: A fluorescence telescope. See the text for the description of the components.

6 Flux measurements

Surface arrays, with its near 100% duty cycle, give the larger data sample used to obtain the energy spectrum. The comparison of the shower energy, measured using fluorescence, with the SD energy parameter for a subset of hybrid events is used to calibrate the energy scale for the array.

The first step towards the flux measurement with the SD array is the reconstruction of arrival direction and core position of air showers. Then, a stable parameter from the SD which correlates with the primary energy is reconstructed. This parameter is the signal at an optimal distances to the shower core at which the spread in the signal size is minimum [55]. In the following we distinguish between *vertical events* ($\theta < 60^\circ$) and *inclined events* ($62^\circ \leq \theta < 80^\circ$). For the case of Auger, the optimal distance is 1000 m for the main array and 450 m for the “infill”, while for TA is 800 m. For *vertical events* the signals at the optimal distance obtained from a LDF fit, have to be corrected for their zenith angle dependence due to air shower attenuation in the atmosphere. This is done in Auger with a Constant Intensity Cut (CIC) method [56]. The equivalent signal at median zenith angle of 38° (35°) is then used to infer the energy for the 1500 m (750 m) array [57, 58]. Events that have independently triggered the SD array and FD telescopes are used for the energy calibration of SD data [59]. The correlation between the different energy estimators and the energy obtained from the FD is shown in Figure 6 (left panel) superimposed with the calibration functions resulting from maximum-likelihood fits. For the case of TA, the energy is estimated by using a look-up table in $S(800)$ and zenith angle determined from an exhaustive Monte Carlo simulation. The uncertainty in energy scale of the Monte Carlo simulation of an SD is large, and possible biases associated with the modelling of hadronic interactions are difficult to determine. Therefore, the SD energy scale is corrected to the TA FD using hybrid events. The observed differences between the FD and SD events are well described by a simple proportionality relationship, where the SD energy scale is 27% higher than the FD [60].

Water Čerenkov detectors from the Pierre Auger Observatory SD, have larger response to inclined showers. These EAS are characterized by the dominance of secondary muons at ground, as the electromagnetic component is largely absorbed in the large atmospheric depth traversed by the shower [61]. The reconstruction is based on the estimation of the relative muon content N_{19} with respect to a simulated proton shower with energy $10 \times 10^{19} \text{eV}$ [62]. N_{19} is used to infer the primary energy for inclined events, as shown in the left pannel of Figure 6.

The energy spectra obtained from the three SD datasets are shown in the right panel of Figure 6. To characterize the spectral features, the Auger collaboration describes the data with a power law below

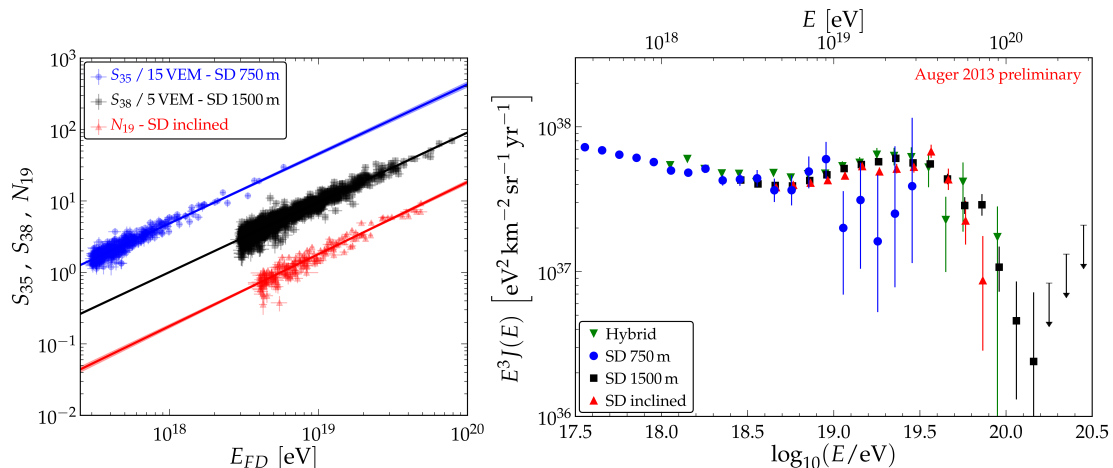


Fig. 6: Left: The correlation between the different energy estimators S38, S35 and N19 (see text) and the energy determined by FD. Right: Energy spectra, corrected for energy resolution, derived from SD and from hybrid data. From Ref. [57].

the ankle $J(E) \propto E^{-\gamma_1}$ and a power law with smooth suppression above:

$$J(E; E > E_a) \propto E^{-\gamma_2} \left[1 + \exp \left(\frac{\log_{10} E - \log_{10} E_{1/2}}{\log_{10} W_c} \right) \right]^{-1}.$$

γ_1, γ_2 are the spectral indices below/above the ankle at E_a . $E_{1/2}$ is the energy at which the flux has dropped to half of its peak value before the suppression, the steepness of which is described with $\log_{10} W_c$. The data in Figure 6 clearly exhibit the ankle at $10^{18.7}$ eV and a flux suppression above $10^{19.6}$ eV. The Pierre Auger Observatory has confirmed the GZK feature of the spectrum with a significance greater than 20σ obtained by comparison to a power law extrapolation. This observation seems to indicate that acceleration in extragalactic sources can explain the high energy CR spectrum, ending the need for exotic alternatives designed to avoid the flux suppression. However, the possibility that this feature in the spectrum is due to the maximum energy of acceleration at the sources is not easily dismissed.

We present here only the energy spectrum from the Pierre Auger Observatory, details of the corresponding spectrum obtained by the Telescope Array collaboration are presented in Ref. [63]. As discussed in Ref. [64], it is found that the energy spectra determined by these experiments are consistent in normalization and shape after energy scaling factors are applied. Those scaling factors are within systematic uncertainties in the energy scale quoted by the experiments.

7 Correlation with astrophysical objects

Since the UHECR are charged particles, they not only lose energy in the interaction with background photons, but also they are deflected by galactic and extragalactic magnetic fields. The galactic magnetic field (GMF) can be modelled as the sum of a regular (large scale fluctuations) and a turbulent (smaller scale fluctuations) components. The directions on the sky in which cosmic rays are deflected strongly depend on the GMF model, however, averaged quantities such as the average UHECR deflection angle are much less model dependent [65]. Extragalactic magnetic fields are expected to be stronger in the large scale structure of the Universe and significantly weaker in voids. UHECR deflections in such fields are poorly constrained ranging from negligible to more than ten degrees, even for 100 EeV protons (See Ref. [26] and references therein). Attempts to detect anisotropies at ultrahigh energies are based on the

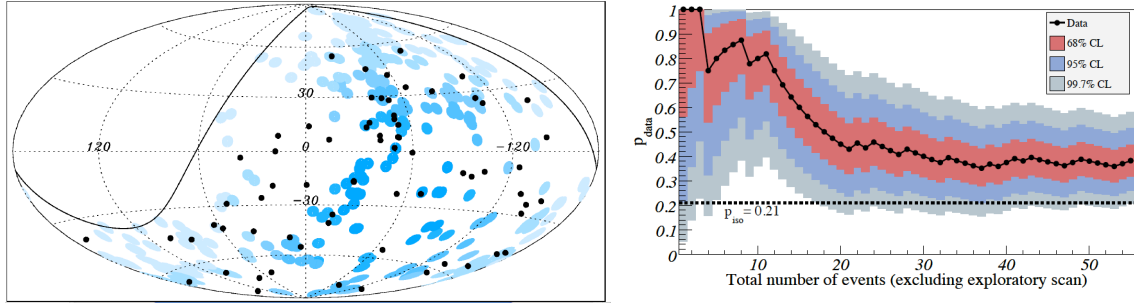


Fig. 7: Left: The 69 arrival directions of cosmic rays with energy $E > 55$ EeV detected by the Pierre Auger Observatory up to December 2009 are plotted as black dots in an Aitoff-Hammer projection of the sky in galactic coordinates. The solid line represents the field of view of the Southern Observatory for zenith angles smaller than 60° . Blue circles of radius 3.1° are centred at the positions of the 318 AGN in the VCV catalogue that lie within 75 Mpc and that are within the field of view of the Observatory. Darker blue indicates larger relative exposure. The exposure-weighted fraction of the sky covered by the blue circles is 21%. Right: Fraction of events correlating with AGN as a function of the cumulative number of events, starting after the exploratory data. The expected correlating fraction for isotropic cosmic rays is shown by the dotted line. From Ref. [68]

selection of events with the largest magnetic rigidity to study whether they can be correlated with the direction of possible sources or distributions of astrophysical objects in our vicinity (less than 100 Mpc).

The most recent discussion of anisotropies in the sky distribution of ultrahigh energy events began when the Pierre Auger Observatory reported a correlation of its highest energy events with AGN [66] in the 12th Veron-Cetty & Veron (VCV) catalogue [67]. To calculate a meaningful statistical significance in such an analysis, it is important to define the search procedure *a priori* in order to ensure it is not inadvertently devised especially to suit the particular data set after having studied it. With the aim of avoiding accidental bias on the number of trials performed in selecting the cuts, the Auger anisotropy analysis scheme followed a pre-defined process. First an exploratory data sample was employed for comparison with various source catalogues and for tests of various cut choices. The results of this exploratory period were then used to design prescriptions to be applied to subsequently gathered data. The first 14 events were used for an exploratory scan and the correlation was most significant for AGN for energy threshold 5.5×10^{19} eV with redshifts $z < 0.018$ (distances < 75 Mpc) and within 3.1° separation angles. The subsequent 13 events established a 99% confidence level for rejecting the hypothesis of isotropic cosmic ray flux. The reported fraction of correlation events was $69_{-13}^{+11}\%$. An analysis with data up to the end of 2009 (69 events in total, as seen in the left panel of Figure 7) indicated that the correlation level decreased to $38_{-6}^{+7}\%$ [68]. In the right panel of Figure 7 we show the most likely value of the fraction of the correlated events with objects in the VCV catalogue as a function of the total number of time-ordered events (the events used in the exploratory scan are excluded). The 1σ and 2σ uncertainties in this value are indicated. The current estimate of the fraction of correlating cosmic rays is $33 \pm 5\%$ (28 events correlating from a total of 84 events) with 21% expected under the isotropic hypothesis [69].

The Telescope Array Collaboration has also searched for correlation with AGN in the VCV catalogue [70, 71]. The TA exposure is peaked in the Northern hemisphere so the AGN visible to TA are not the same as the ones visible to Auger, though there is some overlap. When the distribution of nearby AGN is taken into account, and assuming equal AGN luminosities in UHECR, the correlating fraction would be 40%.

A complete report on the current status for anisotropy searches can be found in [72]. The report includes, in the region around 10^{18} eV, constraints from measuring the first harmonic modulation in the right ascension distribution of arrival directions, and search for point-like sources that would be indicative

of a flux of neutrons (see also Ref. [73]); at higher energies, searches for clustering in arrival directions, and correlations with nearby extragalactic objects (see also Ref. [74]) or the large scale structure of the Universe.

8 Mass composition estimate: the biggest challenge

A determination of primary composition is invaluable in revealing the origin of cosmic rays as this information would provide important bounds on sources and on possible production and acceleration mechanisms. In addition, a proper interpretation of anisotropy information requires knowledge of the primary mass due to the influence on propagation of the galactic and intergalactic magnetic fields. A detailed analysis of composition data from various experiments has been presented in Ref. [75]. We first present a brief description of the general signatures of the EAS (See Ref. [76] for a summary of the phenomenology of these giant air showers). After that, we introduce the shower observables sensitive to primary species.

8.1 Signatures of Extensive Air Showers

The evolution of an extensive air shower is dominated by electromagnetic processes. The interaction of a baryonic cosmic ray with an air nucleus high in the atmosphere leads to a cascade of secondary mesons and nucleons. The first few generations of charged pions interact again, producing a hadronic core, which continues to feed the electromagnetic and muonic components of the showers. Up to about 50 km above sea level, the density of atmospheric target nucleons is $n \sim 10^{20} \text{ cm}^{-3}$, and so even for relatively low energies, say $E_{\pi^\pm} \approx 1 \text{ TeV}$, the probability of decay before interaction falls below 10%. Ultimately, the electromagnetic cascade dissipates around 90% of the primary particle's energy, and hence the total number of electromagnetic particles is very nearly proportional to the shower energy.

By the time a vertically incident 10^{20} eV proton shower reaches the ground, there are about 10^{11} secondaries with energy above 90 keV in the annular region extending 8 m to 8 km from the shower core. Of these, 99% are photons, electrons, and positrons, with a typical ratio of γ to e^+e^- of 9 to 1. Their mean energy is around 10 MeV and they transport 85% of the total energy at ground level. Of course, photon-induced showers are even more dominated by the electromagnetic channel, as the only significant muon generation mechanism in this case is the decay of charged pions and kaons produced in γ -air interactions [77].

It is worth mentioning that these figures dramatically change for the case of very inclined showers. For a primary zenith angle, $\theta > 70^\circ$, the electromagnetic component becomes attenuated exponentially with atmospheric depth, being almost completely absorbed at ground level. As a result, most of the energy at ground level from an inclined shower is carried by muons.

In contrast to hadronic collisions, the electromagnetic interactions of shower particles can be calculated very accurately from quantum electrodynamics. Electromagnetic interactions are thus not a major source of systematic errors in shower simulations. The first comprehensive treatment of electromagnetic showers was elaborated by Rossi and Greisen [78]. This treatment was recently cast in a more pedagogical form by Gaisser [24], which we summarize in the subsequent paragraphs.

The generation of the electromagnetic component is driven by electron bremsstrahlung and pair production [79]. Eventually the average energy per particle drops below a critical energy, ϵ_0 , at which point ionization takes over from bremsstrahlung and pair production as the dominant energy loss mechanism. The e^\pm energy loss rate due to bremsstrahlung radiation is nearly proportional to their energy, whereas the ionization loss rate varies only logarithmically with the e^\pm energy. Throughout this note we take the critical energy to be that at which the ionization loss per radiation length is equal to the electron energy, yielding $\epsilon_0 = 710 \text{ MeV}/(Z_{\text{eff}} + 0.92) \sim 86 \text{ MeV}$ [80]. The changeover from radiation losses to ionization losses depopulates the shower. One can thus categorize the shower development in three phases: the growth phase, in which all the particles have energy $> \epsilon_0$; the shower maximum, X_{max} ; and

the shower tail, where the particles only lose energy, get absorbed or decay.

Most of the general features of an electromagnetic cascade can be understood in terms of the toy model due to Heitler [81]. In this model, the shower is imagined to develop exclusively via bremsstrahlung and pair production, each of which results in the conversion of one particle into two. These physical processes are characterized by an interaction length X_0 . One can thus imagine the shower as a particle tree with branches that bifurcate every X_0 , until they fall below a critical energy, ϵ_0 , at which point energy loss processes dominate. Up to ϵ_0 , the number of particles grows geometrically, so that after $n = X/X_0$ branchings, the total number of particles in the shower is $N \approx 2^n$. At the depth of shower maximum X_{\max} , all particles are at the critical energy, ϵ_0 , and the energy of the primary particle, E_0 , is split among all the $N_{\max} = E_0/\epsilon_0$ particles. Putting this together, we get:

$$X_{\max} \approx X_0 \frac{\ln(E_0/\epsilon_0)}{\ln 2}. \quad (21)$$

Even baryon-induced showers are dominated by electromagnetic processes, so this toy model is still enlightening for such cases. In particular, for proton showers, Eq. (21) tells us that the X_{\max} scales logarithmically with primary energy, while N_{\max} scales linearly. Moreover, to extend this discussion to heavy nuclei, we can apply the superposition principle as a reasonable first approximation. In this approximation, we pretend that the nucleus comprises unbound nucleons, such that the point of first interaction of one nucleon is independent of all the others. Specifically, a shower produced by a nucleus with energy E_A and mass A is modelled by a collection of A proton showers, each with A^{-1} of the nucleus energy. Modifying Eq. (21) accordingly one easily obtains $X_{\max} \propto \ln(E_0/A)$.

Changes in the mean mass composition of the cosmic ray flux as a function of energy will manifest as changes in the mean values of X_{\max} . This change of X_{\max} with energy¹ is commonly known as the elongation rate theorem [82]:

$$D_e = \frac{\delta X_{\max}}{\delta \ln E}. \quad (22)$$

For purely electromagnetic showers, $X_{\max}(E) \approx X_0 \ln(E/\epsilon_0)$ and then the elongation rate is $D_e \approx X_0$. For proton primaries, the multiplicity rises with energy, and thus the resulting elongation rate becomes smaller. This can be understood by noting that, on average, the first interaction is determined by the proton mean free path in the atmosphere, λ_N . In this first interaction the incoming proton splits into $\langle n(E) \rangle$ secondary particles, each carrying an average energy $E/\langle n(E) \rangle$. Assuming that $X_{\max}(E)$ depends logarithmically on energy, as we found with the Heitler model described above, it follows that,

$$X_{\max}(E) = \lambda_N + X_0 \ln[E/\langle n(E) \rangle]. \quad (23)$$

If we assume a multiplicity dependence $\langle n(E) \rangle \approx n_0 E^\Delta$, then the elongation rate becomes,

$$\frac{\delta X_{\max}}{\delta \ln E} = X_0 \left[1 - \frac{\delta \ln \langle n(E) \rangle}{\delta \ln E} \right] + \frac{\delta \lambda_N}{\delta \ln E} \quad (24)$$

which corresponds to the form given in [83],

$$D_e = X_0 \left[1 - \frac{\delta \ln \langle n(E) \rangle}{\delta \ln E} + \frac{\lambda_N}{X_0} \frac{\delta \ln \lambda_N}{\delta \ln E} \right] = X_0 (1 - B). \quad (25)$$

Using the superposition model and assuming that

$$B \equiv \Delta - \frac{\lambda_N}{X_0} \frac{\delta \ln \lambda_N}{\delta \ln E} \quad (26)$$

¹The elongation rate is commonly reported per decade of energy, $D_{10} = \partial \langle X_{\max} \rangle / \partial \log E$, where $D_{10} = 2.3 D_e$.

is not changing with energy, one obtains for mixed primary composition [83]

$$D_e = X_0 (1 - B) \left[1 - \frac{\partial(\ln A)}{\partial \ln E} \right]. \quad (27)$$

Thus, the elongation rate provides a measurement of the change of the mean logarithmic mass with energy.

In Ref. [84], a precise calculation of a hadronic shower evolution has been presented assuming that hadronic interactions produce exclusively pions. The first interaction diverts 1/3 of the available energy ($E_0/3$) into the EM component via the π^0 's, while the remaining 2/3 continue as hadrons. Using pp data [85], we parametrized the charged particle production in the first interaction as $N_{\pi^\pm} = 41.2(E_0/1 \text{ PeV})^{1/5}$. The depth of shower maximum is thus the same as for an electromagnetic shower of energy $E_0/(3N_{\pi^\pm})$, giving for a proton initiated shower:

$$\begin{aligned} X_{\text{max}}^p &= X_0 + X_{\text{EM}} \ln[E_0/(6N_{\pi^\pm}\epsilon_0)] \\ &= (470 + 58 \log_{10}[E_0/1 \text{ PeV}]) \text{ g/cm}^2. \end{aligned} \quad (28)$$

For protons the elongation rate results $\approx 58 \text{ g/cm}^2$ per decade of energy, in good agreement with calculations that model the shower development using the best estimates of the relevant features of the hadronic interactions. Muons are produced from the pion decay when they reach the critical energy (ξ_c^π) after n_c generations. Introducing $\beta = \ln(2N_\pi)/\ln(3N_\pi)$, the total number of muons is:

$$N_\mu = (E_0/\xi_c^\pi)^\beta. \quad (29)$$

For $N_\pi = 5$, $\beta = 0.85$. Unlike the electron number, the muon multiplicity does not grow linearly with the primary energy, but at a slower rate. The precise value of β depends on the average pion multiplicity used. It also depends on the inelasticity of the hadronic interactions. The critical pion energy $\xi_c^\pi \approx 20 \text{ GeV}$ in a shower generated by 1 PeV proton.

Using the superposition model, we obtain for a nucleus of mass A .

$$N_\mu^A = A \left[\frac{(E_0/A)}{\xi_c^\pi} \right]^\beta. \quad (30)$$

From the discussion above, it follows that the depth of shower maximum and the number of muons depend on the mass of the primary particle: iron initiated showers develop faster in the atmosphere, having smaller X_{max} than proton initiated shower, while larger number of muons are expected for heavier nuclei.

While the Heitler model is very useful for imparting a first intuition regarding global shower properties, the details of shower evolution are far too complex to be fully described by a simple analytical model. Full Monte Carlo simulation of interaction and transport of each individual particle is required for precise modelling of the shower development. At present two Monte Carlo packages are available to simulate EAS: CORSIKA (COsmic Ray SIMulation for KAscade) [86] and AIRES (AIR shower Extended Simulation) [87]. Both programs provide fully 4-dimensional simulations of the air showers initiated by protons, photons, and nuclei. A comparative study using these codes can be found in Ref. [88]. Different hadronic interaction models are used in these event generators, such as SIBYLL [89], QGSJET [90] and EPOS [91,92]. The LHC data, particularly those measured in the extreme forward region of the collisions, is of great importance to the physics of EAS. As an example, EPOS has been modified to reproduce in detail LHC data from various experiments [93].

8.2 Measurement of mass sensitive observables

In this section, we discuss how baryonic species may, to some extent, be distinguished by the signatures they produce in the atmosphere. The estimate of primary masses is the most challenging task in high energy cosmic ray physics as such measurements rely on comparisons of data to models. EAS simulations

are subject to uncertainties mostly because hadronic interaction models need to be extrapolated at energy ranges several order of magnitude higher than those accessible to current particle accelerators. In what follows, we consider both surface array and fluorescence detector observables.

The main purpose of fluorescence detectors is to measure the properties of the longitudinal development. The shower longitudinal profile is usually parameterized with a function, such as the Gaisser-Hillas function [94] used by the Pierre Auger Observatory. Using this parameterization, fluorescence detectors can measure X_{\max} with a statistical precision typically around 30 g/cm^2 . The speed of shower development is the clearest indicator of the primary composition. It was shown in Sec. 8 using the superposition model that there is a difference between the depth of maximum in proton and iron induced showers. In fact, nucleus-induced showers develop faster, having X_{\max} higher in the atmosphere. From Monte Carlo simulations, one finds that the difference between the average X_{\max} for protons and iron nuclei is about $90 - 100 \text{ g/cm}^2$. However, because of shower-to-shower fluctuations, it is not possible to obtain meaningful composition estimates from X_{\max} on a shower-by-shower basis, though one can derive composition information from the magnitude of the fluctuations themselves. For protons, the depth of first interaction fluctuates more than it does for iron, and consequently the fluctuations of X_{\max} are larger for protons as well. In Figure 8 the $\langle X_{\max} \rangle$ measurements of $\langle X_{\max} \rangle$ with non-imaging Cherenkov detectors (Tunka [96], Yakutsk [97], CASA-BLANCA [98]) and fluorescence detectors (HiRes/MIA [99], HiRes [100], Auger [101] and TA [102]) compared to air shower simulations using several hadronic interaction models are presented. The conclusion of the detailed study in Ref. [75] indicates that, around the region of the ankle of the cosmic ray spectrum, the measurements are compatible within their quoted systematic uncertainties and the $\langle X_{\max} \rangle$ is close to the prediction for air showers initiated by a predominantly light composition. However, at higher energies, the experimental uncertainties are still too large to draw conclusions from the data. In addition, the systematic differences between different type of measurements are very sensitive to the particular interaction model used for the interpretation.

The electromagnetic component of an EAS suffers more scattering and energy loss than the muonic component and consequently, muons tend to arrive earlier and over a shorter period of time. This means that parameters characterizing the time structure of the EAS, as measured by surface arrays, will be correlated with X_{\max} and hence with primary mass. An early study of the shower signal observed in water Čerenkov detectors arrays [103] established the utility of a shower property known as risetime in estimating the primary composition. Specifically, the risetime, $t_{1/2}$, is defined as the time for the signal to rise from 10% to 50% of the full signal.

In ground array experiments the analysis is usually performed by projecting the signals registered by the detectors into the shower plane (perpendicular to the shower axis) and thus, neglecting the further shower evolution of the late regions. As a consequence, for inclined showers, the circular symmetry in the signals of surface detectors is broken. This results in a dependence of the signal features on the azimuth angle in the shower plane [104, 105]. A detailed study based on Monte Carlo simulations [106], showed that for showers arriving with zenith angle $\theta > 30^\circ$, this is mainly due to the attenuation of the electromagnetic component of the shower as it crosses additional atmosphere to reach a late detector. For a given primary energy E , the risetime asymmetry in water Čerenkov detectors array, as in the Pierre Auger Observatory, depends on zenith angle θ of the primary cosmic ray in such a way that its behaviour versus $\sec \theta$ is reminiscent of the longitudinal development of the shower. In Ref. [106], it was shown that the zenith angle at which the risetime asymmetry becomes maximum, Θ_{\max} , is correlated with the shower development and hence with the primary species.

Using the time information of the signals recorded by the water Čerenkov detectors, it is also possible to obtain information about the longitudinal development of the hadronic component of extensive air showers and the first interaction point in an indirect way. In particular, a method was developed to reconstruct the Muon Production Depth (MPD), the distance to the production of the muon measured parallel to the shower axis, using the signals of detectors far from the core [107]. The MPD technique allows one to convert the time distribution of the signal recorded by the SD detectors into muon produc-

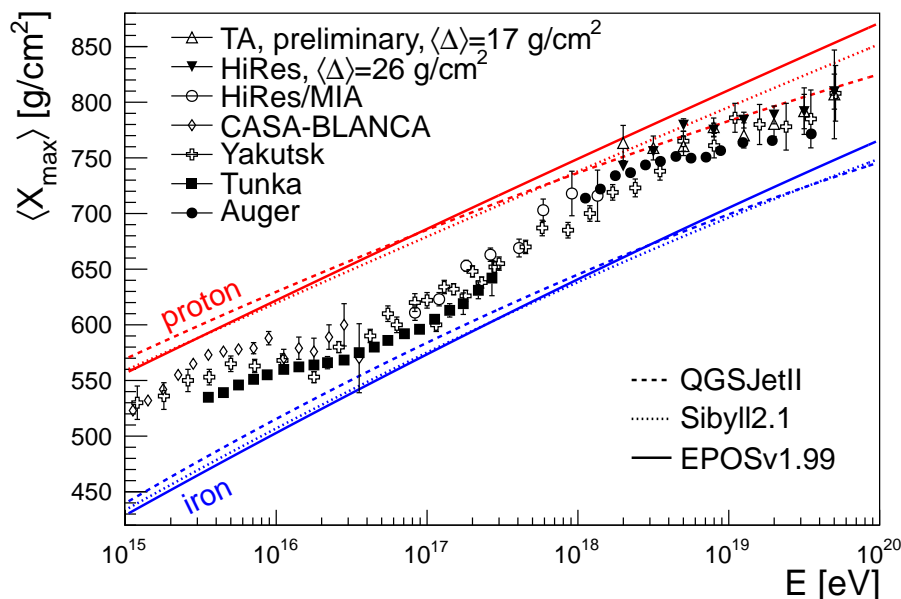


Fig. 8: Measurements of $\langle X_{\max} \rangle$ with non-imaging Cherenkov detectors (Tunka [96], Yakutsk [97], CASA-BLANCA [98]) and fluorescence detectors (HiRes/MIA [99], HiRes [100], Auger [101] and TA [102]) compared to air shower simulations using hadronic interaction models. HiRes and TA data have been corrected for detector effects as indicated by the $\langle \Delta \rangle$ values, to allow comparison with the unbiased measurement from Auger. This picture is taken from Ref. [75].

tion distances using an approximate relation between production distance, transverse distance and time delay with respect the shower front plane. From the MPDs a new observable can be defined, X_{\max}^{μ} , as the depth along the shower axis where the number of produced muons reaches a maximum, which is sensitive to primary mass.

The evolution of X_{\max}^{μ} , Θ_{\max} , $\langle X_{\max} \rangle$ and $\text{RMS}(X_{\max})$ with energy, as measured by the Pierre Auger Observatory with data up to 2010 [108], is presented in Figure 9. For a very complete discussion of these results see Ref. [109]. It is worth noting that these analyses come from completely independent techniques that have different sources of systematic uncertainties. Concerning the RMS, a variety of compositions can give rise to large values of the RMS, because the width of the X_{\max} is influenced by both, the shower-to-shower fluctuations of individual components and their relative displacement in terms of $\langle X_{\max} \rangle$. These measurements from Auger may be interpreted as a transition to a heavier composition that may be caused by a Peters-cycle [110] in extragalactic sources similar to what has been observed at around the knee [75, 109].

Updated studies of X_{\max}^{μ} , $\langle X_{\max} \rangle$ and $\text{RMS}(X_{\max})$ from the Pierre Auger Observatory can be found in Ref. [111]. The most recent results on $\langle X_{\max} \rangle$ measurements from the TA experiment were presented in Refs. [112, 113].

Acknowledgments

I would like to thank the organizers of the 2013 CERN-Latin-American School of HEP for the excellent and stimulating school. I am indebted to Jim Cronin who introduced me to the fascinating world of cosmic rays, he has been an inspiration to me. I also would like to thank Luis Anchordoqui, Luis Epele and John Swain for the many years of fruitful discussions on the phenomenology of EAS and propagation of UHECR *en route* to us from their sources. I am grateful to Hernan Wahlberg, Paul Sommers, Michael

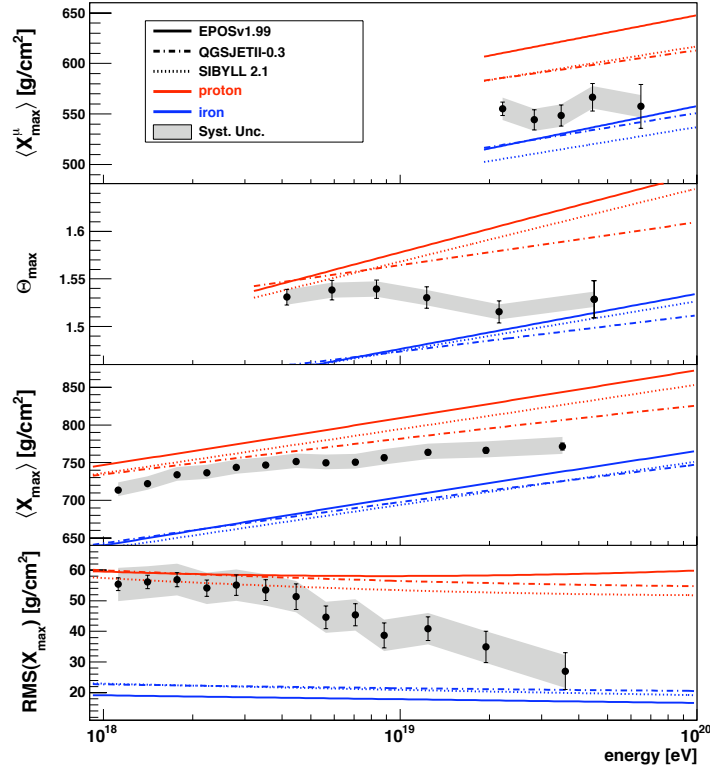


Fig. 9: From top to bottom, $\langle X_{\max}^{\mu} \rangle$, Θ_{\max} , $\langle X_{\max} \rangle$ and $\text{RMS}(\langle X_{\max} \rangle)$ as a function of Energy compared with air shower simulations using different hadronic interaction models. The error bars correspond to the statistical uncertainty, the grey areas correspond to the systematic uncertainty [108]. Updated studies of X_{\max}^{μ} , $\langle X_{\max} \rangle$ and $\text{RMS}(X_{\max})$ can be found in Ref. [111].

Unger, Alan Watson, Analisa Mariazzi, Diego García-Pinto, Fernando Arqueros, Tom Paul and all my colleagues from the Pierre Auger Observatory for lively and enlightening discussions.

References

- [1] V. F. Hess, Phys. Z. 13, 1804 (1912).
- [2] P. Auger, R. Maze, T. Grivet-Meyer, Comptes Rendus 206, 1721 (1938).
- [3] P. Auger, P. Ehrenfest, R. Maze, J. Daudin, Robley, and A. Freon, Rev. Mod. Phys. 11, 288 (1939).
- [4] James W. Cronin, Proceedings of the 30th International Cosmic Ray Conference, Universidad Nacional Autónoma de México, Mexico, Vol. 6, 3-19 (2009).
- [5] M. Kachelriess, Lecture Notes on High Energy Cosmic Rays, 2008, arXiv:0801.4376 [astro-ph].
- [6] L. Anchordoqui, Ultrahigh Energy Cosmic Rays: Facts, Myths, and Legends, 2011, arXiv:1104.0509 [hep-ph].
- [7] J. Beringer *et al.* [Particle Data Group], Phys. Rev. D86, 010001 (2012).
- [8] M. Aglietta *et al.* [EAS-TOP Collaboration], Astropart. Phys. 21, 583 (2004).
- [9] T. Antoni *et al.* [KASCADE Collaboration], Astropart. Phys. 24, 1 (2005).
- [10] W. D. Apel *et al.* [KASCADE Collaboration], Astropart. Phys. 31, 86 (2009).
- [11] W. D. Apel *et al.* [KASCADE-Grande Collaboration], Phys.Rev.Lett.107.171104 (2011)
- [12] A.M. Hillas, arXiv:0607109[astro-ph].
- [13] D. De Marco and T. Stanev, Phys. Rev. D72, 081301 (2005).

- [14] E. Waxman Nucl. Phys. B (Proc. Suppl) 87, 345 (2000).
- [15] V. S. Berezinsky, and S. I. Grigor'eva, Astron. Astrophys. 199, 1 (1988).
- [16] V. Berezinsky, A. Z. Gazizov, and S. I. Grigor'eva, Phys. Rev.D 74, 043005 (2006).
- [17] R. Aloisio, V. Berezinsky, P. Blasi, A. Gazizov, S. Grigor'eva, and B. Hnatyk, Astropart. Phys. 27, 76 (2007).
- [18] D. Allard *et al.* Astron. Astrophys. 443, L29 (2005); D. Allard, E. Parizot, and A. V. Olinto, Astropart. Phys. 27, 61 (2007); D. Allard *et al.* J. Phys. G 34, 359 (2007); D. Allard *et al.* JCAP 0810:033, (2008); C. De Donato, and G. A. Medina Tanco, Astropart. Phys. 32, 253 (2009).
- [19] R. Aloisio, V. Berezinsky and A. Gazizov. Astropart.Phys. 39-40, 129-143 (2012).
- [20] A. M. Hillas, Ann. Rev. Astron. Astrophys. 22, 425 (1984).
- [21] P. Blasi, R.I. Epstein, A. V. Olinto, ApJ Letters, 533, L123 (2000).
- [22] E. Fermi, Phys. Rev. 75, 1169 (1949).
- [23] W. I. Axford, E. Leer, and G. Skadron, International Cosmic Ray Conference, Vol. 11, 132-137 (1977); A. R. Bell, MNRAS 182, 147 (1978); R. D. Blandford and J. P. Ostriker, ApJ Letters, 221, L29 (1978).
- [24] T. K. Gaisser, *Cosmic Rays and Particle Physics*, (Cambridge University Press, 1990).
- [25] R. Blandford, D. Eichler, Phys. Rept. 154, 1-75 (1987).
- [26] K. Kotera, A.V. Olinto, Ann.Rev.Astron.Astrophys. 49, 119-153 (2011).
- [27] A. M. Hillas, Ann. Rev. Astron. Astrophys. 22, 425 (1984).
- [28] M. Lemoine, J.Phys.Conf.Ser. 409, 012007 (2013).
- [29] Waxman E., Bahcall J. Phys. Rev. Lett. 78 2292 (1997).
- [30] Abbasi R. *et al.* [The Ice Cube Collaboration], Nature 484, 351 (2012).
- [31] M. Ahlers, L. A. Anchordoqui, J. K. Becker, T. K. Gaisser, F. Halzen, D. Hooper, S. R. Klein. P. Mészáros, S. Razzaque, and S. Sarkar, FERMILAB-FN-0847-A, YITP-SB-10-01.
- [32] F. W. Stecker, Phys. Rev. Lett. **21**, 1016 (1968).
- [33] V. S. Berezinsky and S. I. Grigor'eva, Astron. Astrophys. 199, 1 (1988).
- [34] R. M. Barnett *et al.* [Particle Data Group], Phys. Rev. D 54, 1 (1996).
- [35] L. Montanet *et al.* [Particle Data Group], Phys. Rev. D 50, 1173 (1994). See p. 1335.
- [36] I. Golyak, Mod. Phys. Lett. A **7**, 2401 (1992).
- [37] L. A. Anchordoqui, M. T. Dova, L. N. Epele and J. D. Swain, Phys. Rev. D55, 7356 (1997).
- [38] J. L. Puget, F. W. Stecker and J. H. Bredekamp, Astrophys. J. 205, 638 (1976).
- [39] M. J. Chodorowski, A. A. Zdziarski, and M. Sikora, Astrophys. J.400, 181 (1992).
- [40] S. Michalowski, D. Andrews, J. Eickmeyer, T. Gentile, N. Mistry, R. Talman and K. Ueno, Phys. Rev. Lett. 39, 737 (1977).
- [41] F. W. Stecker, Phys. Rev. 180, 1264 (1969).
- [42] M. A. Malkan and F. W. Stecker, Astrophys. J. 496 13(1998).
- [43] L. A. Anchordoqui, M. T. Dova, L. N. Epele and J. D. Swain, Phys. Rev. D 57, 7103 (1998).
- [44] F. W. Stecker and M. H. Salamon, Astrophys. J. 512, 521 (1992).
- [45] L. N. Epele and E. Roulet, JHEP 9810, 009 (1998).
- [46] Allard, D. Astropart. Phys 39-40, 33-43 (2012).
- [47] Mucke A., Engel R., Rachen J. P., Protheroe R. J., and Stanev T., Comp. Phys. Com., 124, 290 (2000).
- [48] Armengaud, E., Sigl, G., and Miniati, F., Phys. Rev. D, 73, 083008 (2006).
- [49] D. Allard, M. Ave., N. Busca *et al.* JCAP, 9, 5 (2006).
- [50] J. Abraham *et al.* [Pierre Auger Collaboration], Nucl. Instrum. Meth. A **523**, 50 (2004).

- [51] T Abu-Zayyad *et al.* [TA Collaboration], Nucl. Instr. Meth. A689, 87 (2012).
- [52] J. Abraham *et al.* [Pierre Auger Collaboration], Nucl. Instrum. Meth.A 620, 227 (2010).
- [53] T. Hermann-Josef Mathes [Pierre Auger Collaboration], Proc. 32nd International Cosmic Ray Conference (ICRC 11), Beijing, China 3, 149 (2011).
- [54] D. Ivanov, B.T. Stokes *et al.* Proc. 32nd International Cosmic Ray Conference, 1297 (2011).
- [55] A.M. Hillas, Acta Physica Academiae Scientiarum Hungaricae 26, 355 (1970).
- [56] J. Hersil *et al.* Phys. Rev. Lett. 6, 22 (1961).
- [57] A. Schulz [Pierre Auger Collaboration], to appear in Proc. 33rd International Cosmic Ray
- [58] J. Abraham *et al.* [Pierre Auger Collaboration], Phys. Rev. Lett. 101, 061101(2008). R. Pesce [Pierre Auger Collaboration], Proc. 32nd International Cosmic Ray Conference (ICRC 11), Beijing, China (2011).
- [59] Conference (ICRC 13), Brasil (2013), arXiv:1307.5059[astro-ph].
- [60] T. Abu-Zayyad *et al.* ApJ768, L1 (2013).
- [61] I. Valino [Pierre Auger Collaboration], Proc. 31st International Cosmic Ray Conference (ICRC 09), Łódź, Poland (2009).
- [62] G. Rodriguez [Pierre Auger Collaboration], UHECR Symposium CERN (2012), EPJ Web Conf.53: 07003 (2013); I. Valino [Pierre Auger Collaboration] to appear in Proc. 33rd International Cosmic Ray Conference (ICRC 13), Brasil (2013).
- [63] O.E. Kalashev, E. Kido and the Telescope Array Collaboration, to appear in Proc. 33rd International Cosmic Ray Conference (ICRC 13), Brasil (2013).
- [64] B. Dawson, *et al.* [Pierre Auger, Telescope Array and Yakutsk Collaborations] Working Group report at UHECR Symposium CERN (2012), EPJ Web Conf.53: 01005 (2013).
- [65] G. Giacinti, M. Kachelriess, D. Semikoz and G. Sigl, G \S nter. EPJ Web Conf. 53: 06004 (2013).
- [66] J. Abraham *et al.* [Pierre Auger Collaboration], Science 318 (5852), 938 (2007); J. Abraham *et al.* [Pierre Auger Collaboration], Astropart. Phys. 29, 188 (2008) [Erratum-ibid. 30, 45 (2008)].
- [67] M.-P. Veron-Cetty & P. Veron, Astron. Astrophys. 455, 773 (2006).
- [68] P. Abreu *et al.* [Pierre Auger Collaboration], Astropart. Phys. 34, 314 (2010)
- [69] K.-H. Kampert [Pierre Auger Collaboration], Proc. 32nd International Cosmic Ray Conference (ICRC211), Beijing (2011).
- [70] Abu-Zayyad, *et al.* Astrophys.J.757, 26 (2012).
- [71] M. Fukushima *et al.* [TA Collaboration], to appear in Proc. 33rd International Cosmic Ray Conference, Rio de Janeiro, Brazil (2013).
- [72] O. Deligny *et al.* [Pierre Auger, Yakutsk and Telescope Array Collaborations], Working Group report at UHECR Symposium CERN (2012), EPJ Web Conf.53:01008 (2013).
- [73] A. AAb *et al.* [Pierre Auger Collaboration], ApJ. 760, 148 (2012).
- [74] A. AAb *et al.* [Pierre Auger Collaboration], JCAP 05, 009 (2013)
- [75] K-H. Kampert and M. Unger, Astropart.Phys. 35, 660 (2012).
- [76] L. Anchordoqui, M. T. Dova, A. G. Mariazzi, T. McCauley, T. C. Paul, S. Reucroft and J. Swain, Annals Phys. 314, 145 (2004).
- [77] T. J. L. McComb, R. J. Protheroe and K. E. Turver, J. Phys. G 5, 1613 (1979).
- [78] B. Rossi and K. Greisen, Rev. Mod. Phys. 13, 240 (1941).
- [79] H. Bethe and W. Heitler, Proc. Roy. Soc. Lond. A 146, 83 (1934).
- [80] B. Rossi, *High Energy Particles* (Prentice-Hall, Inc., Englewood Cliffs, NY, 1952).
- [81] W. Heitler. *The Quantum Theory of Radiation*, 2nd. Edition, (Oxford Univ. Press, London, 1944).
- [82] J. Linsley. Proc. 15th International Cosmic Ray Conference, Plovdiv 12, 89 (1977).

- [83] J. Linsley and A. A. Watson, Phys. Rev. Lett. 46, 459 (1981).
- [84] J. Matthews, Astropart. Phys. 22, 387 (2005).
- [85] C. AMSLER *et al.* [Particle Data Group], Phys. Lett. B 667, 1 (2008).
- [86] D. Heck, G. Schatz, T. Thouw, J. Knapp and J. N. Capdevielle, FZKA-6019 (1998).
- [87] S. J. Sciutto, arXiv:9911331[astro-ph].
- [88] J. Knapp, D. Heck, S. J. Sciutto, M. T. Dova and M. Risse, Astropart. Phys. 19, 77 (2003).
- [89] R. S. Fletcher, T. K. Gaisser, P. Lipari and T. Stanev, Phys. Rev. D 50, 5710 (1994).
- [90] N. N. Kalmykov, S. S. Ostapchenko and A. I. Pavlov, Nucl. Phys. Proc. Suppl. 52B, 17 (1997).
- [91] K. Werner, F.-M. Liu, and T. Pierog, Phys. Rev. C74, 044902 (2006).
- [92] T. Pierog and K. Werner, Nucl. Phys. Proc. Suppl. B 196,102 (2009).
- [93] T. Pierog, Iu Karpenko, J.M. Katzy, E. Yatsenko and K. Werner, arXiv:1306.0121[hep-ph].
- [94] T. K. Gaisser and A. M. Hillas. Proc. of 15th International Cosmic Ray Conference, Plovdiv 8, 353 (1977).
- [95] E. Barcikowski *et al.* [HiRes, Pierre Auger, Telescope Array and Yakutsk Collaborations] Proc. of Int. Symposium on Future Directions in UHECR Physics (UHECR2012), CERN, Switzerland, EPJ Web Conf. 53:01006 (2013).
- [96] N. Budnev *et al.*, [Tunka Collaboration] Nucl. Phys. (Proc. Suppl.) 190, 247(2009); V. Prosin *et al.* [Tunka Coll.], Proc. 32nd International Cosmic Ray Conference, Beijing, China, vol. 1, 197 (2011).
- [97] S. Knurenko, A. Sabourov [Yakutsk Collaboration], in: Proceedings XVI ISVHECRI, 2010; S. Knurenko, A. Sabourov, [Yakutsk Collaboration], Nucl. Phys. B (Proc. Suppl.)212, 241 (2011).
- [98] J. Fowler *et al.* [CASA-BLANCA Collaboration], Astropart. Phys. 15, 49 (2001).
- [99] T. Abu-Zayyad *et al.* [HiRes/MIA Collaborations], Astrophys. J. 557, 686 (2001).
- [100] R. Abbasi *et al.* [HiRes collaboration], Phys. Rev. Lett. 104, 161101 (2010).
- [101] P. Facal *et al.* [Pierre Auger Collaboration] Proc. 32nd International Cosmic Ray Conference, Beijing, China, vol. 2, 105 (2011).
- [102] C. Jui *et al.* [TA Collaboration], Proceedings APS DPF Meeting, arXiv:1110.0133[astro-ph].
- [103] A. A. Watson and J. G. Wilson, J. Phys. A 7, 1199 (1974).
- [104] M. T. Dova [Pierre Auger Collaboration], Proc. 28th International Cosmic Ray Conference, Tsukuba, 369 (2003), arXiv:0308399[astro-ph].
- [105] M. T. Dova, L. N. Epele and A. G. Mariazzi, Astropart. Phys. 18, 351 (2003).
- [106] M. T. Dova, M. E. Manceñido, A. G. Mariazzi, H. Wahlberg, F. Arqueros and D. García-Pinto, Astroparticle Phys. 31, 312 (2009).
- [107] L. Cazon, R.A. Vazquez and E. Zas, Astropart. Phys. 23: 393-409 (2005); L. Cazon, R. Conceicao, M. Pimenta, E. Santos, Astropart. Phys. 36, 211 (2012).
- [108] D. García-Pinto [Pierre Auger Collaboration], Proc. 32nd International Cosmic Ray Conference, Beijing, China (2011).
- [109] M. Unger [Pierre Auger Coll.], Proc. of Int. Symposium on Future Directions in UHECR Physics (UHECR2012), CERN, Switzerland, EPJ Web Conf., 53:04009 (2013).
- [110] B. Peters, Nuovo Cimento 22, 800 (1961).
- [111] A. Aab [Pierre Auger Collaboration], to appear in Proc. 33rd International Cosmic Ray Conference, Rio de Janeiro, Brazil (2013), arXiv:1307.5059[astro-ph].
- [112] W. Hanlon [TA Collaboration], to appear in Proc. 33rd International Cosmic Ray Conference, Rio de Janeiro, Brazil (2013).
- [113] Y. Tameda [TA Collaboration], to appear in Proc. 33rd International Cosmic Ray Conference, Rio de Janeiro, Brazil (2013).